Monthly Notices of the ROYAL ASTRONOMICAL SOCIETY

MNRAS **533,** 4234–4247 (2024) https://doi.org/10.1093/mnras/stae1998
Advance Access publication 2024 August 21

ATOMS: ALMA three-millimetre observations of massive star-forming regions – XVI. Neutral versus ion line widths

C. Zhang,[1,2]★ Tie Liu,[3]★ Z.-Y. Ren,[4]★ Feng-Yao Zhu,[5] H.-L. Liu,[6] Ke Wang,[7] J.-W. Wu,[8,4] D. Li,[9,4,10] Sihan Jiao,[4] K. Tatematsu,[11,12] Mika Juvela,[13] Chang Won Lee,[14,15] Wenyu Jiao,[3] Leonardo Bronfman,[16] Jianwen Zhou,[17] Feng-Wei Xu,[18,19,20] Anandmayee Tej,[21] Jihye Hwang,[14] Archana Soam,[22] Swagat Das[16] and James O. Chibueze[23,24,25]

Affiliations are listed at the end of the paper

Accepted 2024 August 16. Received 2024 August 16; in original form 2024 May 5

ABSTRACT

It has been suggested that the line width of ions in molecular clouds is narrower than that of the co-existing neutral particles, which has been interpreted as an indication of the decoupling of neutral turbulence from magnetic fields within a partially ionized environment. We calculate the principal component analysis (PCA) correlation coefficients of CCH versus $H^{13}CO^+$ and $H^{13}CN$ versus $H^{13}CO^+$. We find aside from $H^{13}CN$, CCH could also be strongly spatial correlated with $H^{13}CO^+$ in high-mass star-forming regions. CCH and $H^{13}CO^+$ line emissions are strongly spatial correlated with each other in 48 per cent sources with a PCA correlation coefficient over 0.7. So, we investigate the ambipolar diffusion (AD) effect using CCH and $H^{13}CO^+$ lines as a neutral/ion pair in a sample of 129 high-mass star-forming clumps. We conduct a careful analysis of line widths of the CCH–$H^{13}CO^+$ pair pixel-by-pixel in 12 sources, which show a strong correlation in CCH–$H^{13}CO^+$ emission and no obvious outflows or multiple velocity components. The mean velocity dispersion of CCH is about the same as $H^{13}CO^+$ in 12 sources. In low-density regions of most sources, CCH shows a broader velocity dispersion than $H^{13}CO^+$. However, the AD effect is not significant from a statistical point of view.

Key words: ISM: clouds.

1 INTRODUCTION

Magnetic fields (B-fields) and turbulent flows are ubiquitous in the Milky Way and are believed to play various important roles in converting gas into stars (Klaassen 2008). In most analyses and numerical simulations, turbulent flows and B-fields are treated as perfectly coupled (Tang, Li & Lee 2018). This constitutes a reasonably accurate approximation when examining large-scale phenomena. However, at smaller scales, the decoupling between neutral flows and magnetic fields, also known as ambipolar diffusion (AD), becomes inevitable (Mouschovias 1987; Zweibel 2002; Li & Houde 2008; Li et al. 2010). AD represents the physical mechanism characterizing the relative motion of neutral and charged particles along magnetic field lines within partially ionized environments. Turbulent AD at smaller scales may also augment the efficiency of large-scale mean-field AD (Fatuzzo & Adams 2002; Zweibel 2002; Heitsch et al. 2004; Nakamura & Li 2005), and the friction between ions and neutrals may accelerate the dissipation of turbulent energy (e.g. Mouschovias & Tassis 2008). Turbulence dissipation and mean-field AD are both critical in the process of mass condensation, with the scale of turbulent AD being an important parameter in star formation.

Li & Houde (2008) proposed that turbulent AD can induce differences between the velocity dispersions of coexistent ions and neutrals, as measured through spectral line widths. This occurs because the line width is determined not solely by the contributions of turbulent eddies at scales similar to the beam size, but also by the cumulative effect of all smaller eddies within that scale. To discern this nuanced effect, it is essential to employ a pair of neutral and ion tracers that sample very similar volumes within a molecular cloud, thereby minimizing the impact of extraneous variables. Houde et al. (2000) compared single-dish observations of neutrals and ions for which they see a broader line width for neutrals compared to ions, and derived a relation for the line widths of the ions and neutrals. Their approach accounts for collisions between ions and neutrals as individual particles, based on the premise that ions are subject to gyromagnetic motion around the magnetic field's axis. With these assumptions, it is inevitable that ions will demonstrate a narrower line width when charting the same spatial area. This claim is further developed and verified by later works such as Hezareh et al. (2010, 2014) and Tang et al. (2018).

However, some observational evidence show that their finding is at odds with the conventional theoretical picture (Tafalla et al. 2004; Sokolov et al. 2019; Pineda et al. 2021). Pineda et al. (2021) compared the velocity dispersion of ions and neutrals in the dense core Barnard

★ E-mails: zhangchao920610@126.com (CZ); liutie@shao.ac.cn (TL); renzy@nao.cas.cn (Z-YR)

Table 1. The basic observational parameters.

Molecule	Transition	Rest frequency (GHz)	Sensitivity (mJy beam^{-1} MHz^{-1})	Beam sizes (arcsec)	Spectral resolutions (km s^{-1})	rms of intensity (mJy beam^{-1} km s^{-1})
$H^{13}CO^+$	1–0	86.754288	∼80	∼2	∼0.2	∼3
$H^{13}CN$	1–0	86.339918	∼80	∼2	∼0.2	∼1
CCH	1–0	87.316898	∼80	∼2	∼0.2	∼2

5 and found the non-thermal velocity dispersion of the ion traced by N_2H^+ is systematically higher than that of the neutrals traced by NH_3. This observed variation may indicate that the magnetic field continues to fluctuate even within the depths of the dense core, akin to the turbulent regions outside the core. Ions are likely to exhibit a stronger dynamic coupling with this fluctuating field in comparison to neutrals, thereby accounting for their broader spectral line widths. However, the tracers (N_2H^+ and NH_3) used in their work have very different critical densities, and may trace different density layers of the dense core.

To investigate the AD effect more properly, it is better to use a neutral/ion pair tracing a similar volume of the cloud, with similar critical densities. In this work, we compared the line widths of a neutral/ion pair, CCH (1−0) and $H^{13}CO^+$ (1−0), which have similar critical densities. The critical densities of CCH (1−0) and $H^{13}CO^+$(1−0) are 1×10^5 cm^{-3} and 2×10^5 cm^{-3} at 30 K (Pety et al. 2017). This comparison was undertaken in a large sample of high-mass star-forming regions, using the high-resolution data obtained from the ATOMS (ALMA Three-millimetre Observations of Massive Star-forming regions) survey programme.

2 OBSERVATIONS

We made the ALMA observations for 146 active Galactic star-forming regions as the ATOMS survey. These 146 sources were selected from the CS J = 2−1 survey of Bronfman, Nyman & May (1996). The sample of 146 targets is complete for proto-clusters with bright CS J = 2−1 emission (T_b> 2 K), indicative of reasonably dense gas. The overall properties of these 146 targets are shown in table A of Liu et al. (2020a). Most (139) of the targets are located in the first and fourth Galactic quadrants of the inner Galactic plane. The distances of the sample clouds range from 0.4 to 13.0 kpc with a mean value of 4.5 kpc. The sample includes 27 distant (d>7 kpc) sources that are either close to the Galactic centre or mini-starbursts, representing extreme environments for star formation. The properties of these sources have been described in detail in Liu et al. (2016, 2020a, b, 2021).

Images were made from the 12-m and Atacama Compact Array (ACA) visibility data jointly. Fully calibrated visibility data were generated by running the ALMA Pipeline, which applies calibration tables obtained from the Quality Assurance 2 (QA2) to the raw data. Line images were made for each spectral window (SPW) with native spectral resolution. The 12-m and ACA array data were calibrated independently. Subsequently, the visibility data from both the 12-m and ACA array configurations were merged and imaged using the Common Astronomy Software Applications (CASA). For each source and SPW, a line-free frequency range is automatically identified through the ALMA pipeline, as detailed in the ALMA Technical Handbook. This frequency range serves to (a) eliminate the continuum from line emission in the visibility domain, and (b) create continuum images. The continuum images are generated through multifrequency synthesis of data within these line-free frequency ranges in the two 1.875 GHz wide spectral windows, specifically SPWs 7 and 8, which are centred around approximately 99.4 GHz (or 3 millimetres). Visibility data from both the 12-m and ACA arrays are jointly deconvolved using the task TCLEAN in CASA version 5.6. Natural weighting and a multiscale deconvolution approach are employed to optimize sensitivity and image quality. All resulting images are corrected for the primary beam. The details of data reduction are described in Zhou et al. (2022). The 12-m and ACA combined data have a synthesized beam size of ∼2 arcsec.

There are 129 sources that all display emission in the spectral lines of $H^{13}CO^+$ (1−0), $H^{13}CN$ (1−0), and CCH (1−0) in ATOMS survey. The spectral and angular resolutions of the spectral lines for CCH, $H^{13}CN$, and $H^{13}CO^+$ are all around 0.2 km s^{-1} and 2 arcsec, respectively. For each source, we initially plot the spectral lines to ascertain the required velocity range. The velocity intervals of the three spectral lines are essentially identical. Spectral lines falling within a range of 3 times the root mean square (rms) are excluded. We smooth the data cube to a uniform angular resolution and regrid it to the same as the $H^{13}CO^+$ (1−0) transition. Subsequently, an intensity map is derived by integrating over the specified velocity range. We obtained the integrated intensity maps of $H^{13}CO^+$, $H^{13}CN$, and CCH using the CASA software. The noise levels of the integrated intensity of $H^{13}CO^+$, $H^{13}CN$, and CCH are estimated as 3, 1, 2 mJy beam^{-1} km s^{-1} within the emission-free regions in the intensity maps, respectively. All the basic observational parameters are summarized in the Table 1.

3 RESULTS

3.1 Principal component analysis

Principal component analysis (PCA) is a statistical procedure to convert a set of observations of possibly correlated variables into a set of values of linearly uncorrelated variables called principal components. PCA has been widely used to identify and quantify similarities and differences between various molecular line emissions inside molecular clouds (Lo et al. 2009; Jones et al. 2012, 2013; Liu et al. 2020a). For the 129 sources, we performed PCA on the pairs of integrated emission maps of $H^{13}CN$–$H^{13}CO^+$ and CCH–$H^{13}CO^+$ to characterize their differences in spatial distribution following a similar procedure in Liu et al. (2020a). The integrated intensity maps of an exemplar source (I13291-6229) are presented in Fig. 1. These maps were first smoothed and gridded to ensure that they have the same angular resolution and pixel sizes. We then exported their pixel values for PCA analysis.

In the example source I13291-6229, the PCA correlation coefficient of CCH–$H^{13}CO^+$ and $H^{13}CN$–$H^{13}CO^+$ are 0.76 and 0.77. It indicates that both CCH and $H^{13}CN$ show strong correlations with $H^{13}CO^+$, suggesting that these molecules have very similar spatial distributions. Fig. 2 shows the distribution of PCA correlation coefficients of $H^{13}CN$–$H^{13}CO^+$ and CCH–$H^{13}CO^+$ pairs. The blue and orange represent CCH and $H^{13}CN$, respectively. It shows that the PCA correlation coefficients of $H^{13}CN$–$H^{13}CO^+$ are slightly higher than that of CCH–$H^{13}CO^+$ in general, which indicates that the spatial

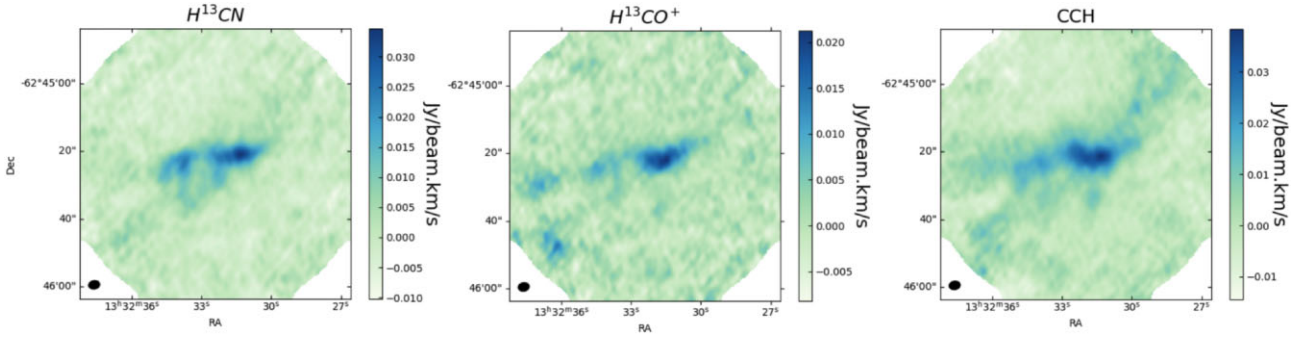

Figure 1. The integrated intensity maps of the exemplar source I13291-6229. Intensity maps for $H^{13}CN$, $H^{13}CO^+$, and CCH are shown in the left, middle, and right panels, respectively. Each panel's corresponding colour bar delineates the intensity values.

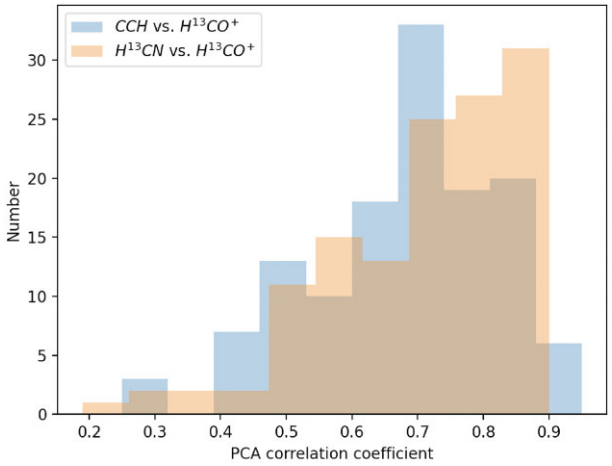

Figure 2. The distribution of PCA correlation coefficients of $H^{13}CN$–$H^{13}CO^+$ (orange histogram) and CCH–$H^{13}CO^+$ (blue histogram) pairs.

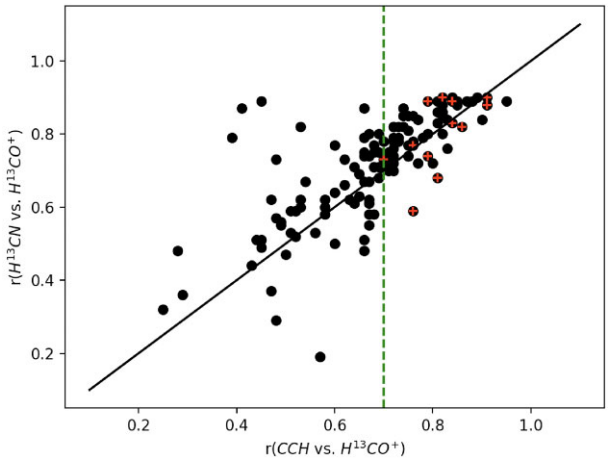

Figure 3. The correlation between the PCA correlation coefficients of CCH versus $H^{13}CO^+$ pair and $H^{13}CN$ versus $H^{13}CO^+$ pair. The black line marks the one-to-one relation. The green dashed line shows the PCA correlation coefficient of CCH–$H^{13}CO^+$ of 0.7. The sources in Table 2 are marked with red crosses.

distributions of the $H^{13}CN$–$H^{13}CO^+$ pair has a better correlation than the CCH–$H^{13}CO^+$ pair. For the $H^{13}CN$, 64 per cent sources have PCA correlation coefficients over 0.7, 77 per cent sources over 0.6 and 92 per cent sources over 0.5. For the CCH, there are 48 per cent sources that have PCA correlation coefficients over 0.7, 74 per cent sources over 0.6 and 87 per cent sources over 0.5. Previous studies have demonstrated significant variations in the spatial distributions of CCH and $H^{13}CO^+$ within the Orion B molecular cloud (Pety et al. 2017). Our analysis suggests that CCH could also be strongly correlated with $H^{13}CO^+$ in high-mass star-forming regions.

Fig. 3 presents the correlation between the PCA correlation coefficients of CCH–$H^{13}CO^+$ pair and $H^{13}CN$–$H^{13}CO^+$ pair. The black line marks the one-to-one correlation. It can be seen that when the correlation coefficient of CCH–$H^{13}CO^+$ is greater than 0.7 (the green dotted line), the PCA coefficient of CCH–$H^{13}CO^+$ pair and $H^{13}CN$–$H^{13}CO^+$ pair is distributed around the one-to-one line. This indicates that for sources with correlation coefficients over 0.7, the three line tracers, $H^{13}CN$, $H^{13}CO^+$, and CCH, are strongly spatial correlated with each other. This is also evidenced in their integrated intensity maps (Fig. 1), showing that $H^{13}CN$, $H^{13}CO^+$, and CCH have quite similar emission distribution.

3.2 Velocity dispersion measurement

Although the $H^{13}CN$ shows a stronger correlation with $H^{13}CO^+$ than CCH, the hyperfine structure of $H^{13}CN$ (1−0) line emission makes it difficult to accurately measure its line width. As discussed in last section, CCH in general is also well correlated with $H^{13}CO^+$ in high-mass star formation regions of the ATOMS sample. In addition, $H^{13}CO^+$ (1−0) and CCH (1−0) have similar critical densities (Pety et al. 2017). Therefore, we decided to use CCH and $H^{13}CO^+$ as a neutral/ion pair in the study of the AD effect in this work. We focus on those sources in which $H^{13}CN$, $H^{13}CO^+$, and CCH show very similar spatial distribution, with correlation coefficients over 0.7. There are 62 sources with correlation coefficients over 0.7.

Outflows and multiple velocity components can also broaden line widths and largely affect the measuring of line widths in some sources. Therefore, we picked out 12 sources out of the 62 sources, where CCH and $H^{13}CO^+$ do not show correlation with the outflows and dominated by one velocity component. However, we can only rule out the cases where there are obvious multiple emission peaks. When a spectral line indicates the presence of multiple velocity components, the line width obtained from a single Gaussian fit tends to be broader than necessary. For each source, we determine a threshold by observing the line widths in both the central and peripheral regions of the molecular cloud, and then exclude areas where the fitted line width exceeds this threshold (around 1.5 to 2 km s^{-1}). Subsequently, we randomly select several points, marked with red dots as numbers one to nine in Fig. 4, to assess the reasonableness of this approach. The selection of these points is

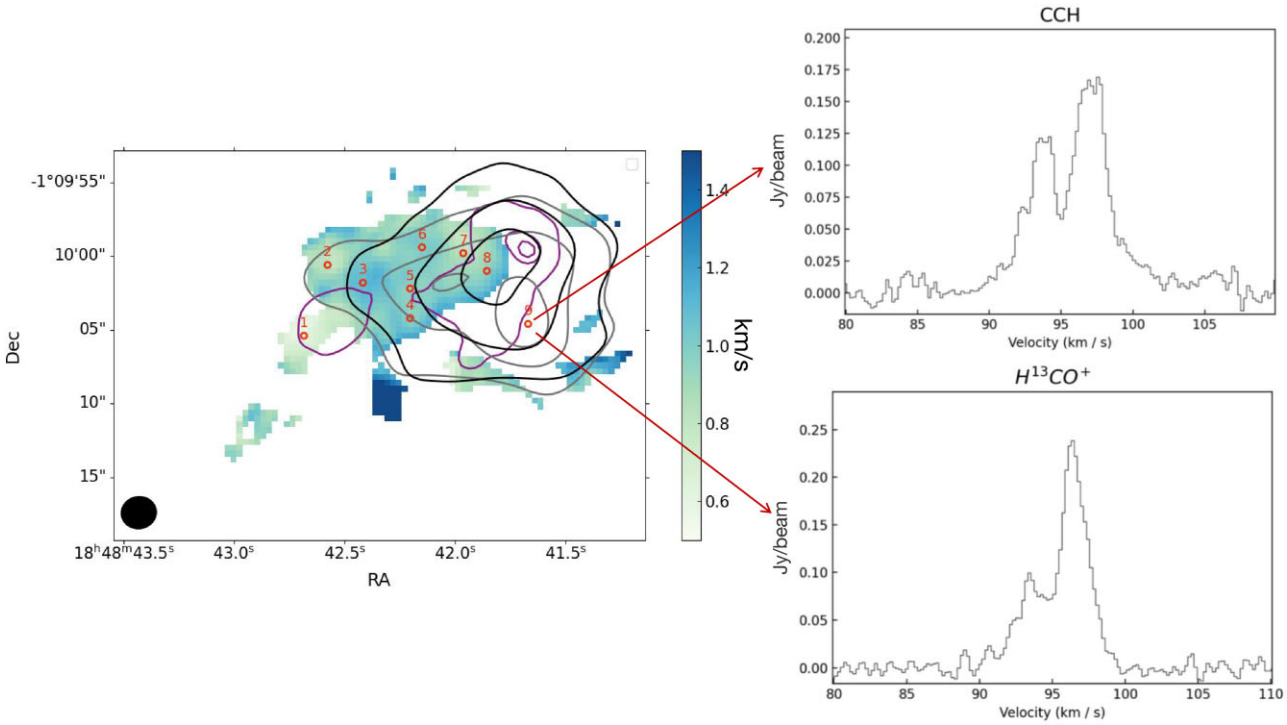

Figure 4. Source I18461-0113. *Left*: Ratio of the velocity dispersion between CCH and $H^{13}CO^+$(R(CCH/$H^{13}CO^+$)). The black and grey contours are shown for the $H^{13}CO^+$ and CCH integrated intensity map, respectively. The contour levels are drawn at 40 per cent, 70 per cent, and 90 per cent of peak values. The purple contour is shown for the 3 mm continuum emission. The contour levels are drawn at 30 per cent, 70 per cent, and 90 per cent of peak values. In the online materials, we have provided spectra for CCH and $H^{13}CO^+$ corresponding to the numbers one to eight. *Right*: The spectrum of the region numbered as nine within left panel. The spectra is excluded due to the multiple components in analysis.

random but spans areas from the interior to the exterior of the molecular cloud. For instance, the left panel of Fig. 4 offers a detailed comparison of the velocity dispersion ratios for CCH and $H^{13}CO^+$ concerning the particular source I18461-0113. The right panel displays the spectrum corresponding to the region numbered nine in the left panel, where the spectra reveal distinct multiple velocity components that are further elaborated in the left panel. The online materials include spectra for CCH and $H^{13}CO^+$ corresponding to numbers one to eight. In the case of I16272-4837, the spectra show a dominant velocity component compared to the other (see fig. E1 of Xu et al. 2023), which can be well-fitted with two Gaussian components in both two species. We carefully checked all the spectra across all maps in the 12 sources and excluded the pixels that show multiple velocity components such as the source in Fig. 4 right panel.

We perform the Gaussian fit for both lines, $H^{13}CO^+$ and CCH, pixel-by-pixel using PYSPECKIT. Fig. 5 shows two exemplar spectrum of source I18461-0113. Left and right panels show the CCH and $H^{13}CO^+$, respectively. The value and error of Gaussian fits parameters are shown in the upper right in each panel. The uncertainties of line width from the fitting procedure for CCH and $H^{13}CO^+$ span the intervals of 0.009 to 0.031 km s^{-1} and 0.014 to 0.071 km s^{-1}, respectively. Compared to the spectral resolution (around 0.2 km s^{-1}) and typical line widths (around 1.5 km s^{-1}) for CCH and $H^{13}CO^+$, the uncertainties in the line width measurements are small. In general, the Gaussian fits provide a good estimation of the line widths.

The comparison between CCH and $H^{13}CO^+$ are shown in Fig. 6. The right panel shows the comparison of the centroid velocity obtained for both tracers using kernel density estimation (KDE), which agrees within 1.5 km s^{-1}. This comparison shows that there is not a single velocity offset between the different tracers. The left panel shows the difference in velocity maps between the CCH and $H^{13}CO^+$. This map shows that CCH display mostly lower centroid velocities than $H^{13}CO^+$, but that in a few regions the relation is the reverse, although without a clear spatial trend.

3.3 Velocity dispersion error

Potential variations in noise levels within the CCH and $H^{13}CO^+$ intensity maps may influence the line width. To assess the impact of these variations on the line width, we utilize corner plots, which illustrate the posterior distribution of the statistical model. We have generated a Gaussian spectral line with an amplitude A of 0.1143 Jy beam^{-1} km s^{-1} and a line width of 0.8 km s^{-1}, derived from actual spectral fitting as shown in Fig. 7(a). By incorporating different noise levels, we can evaluate the effect of noise on the line width fitting. As detailed in Section 2, the noise levels for the CCH and $H^{13}CO^+$ intensity maps are approximately 2 and 3 mJy beam^{-1} km s^{-1}, respectively. White noise levels of 1.5 and 3.5 mJy beam^{-1} km s^{-1} are added to the Gaussian line to observe the impact of noise levels on the line width fitting under maximum variance conditions. Fig. 7(b) displays the Gaussian line with added white noise. Figs 7(c) and (d) present the corner maps. In the corner maps, the histogram represents the measure of fit deviation when the parameters are randomly sampled near the best-fit. Here, we use likelihood as the measure. The green solid line indicates the best-fit, while the purple dashed lines represent the 16 per cent, 50 per cent (median), and 84 per cent confidence interval percentiles. The subtitles on the histograms display the estimated values for each parameter along with the Gaussian errors at the 68 per cent

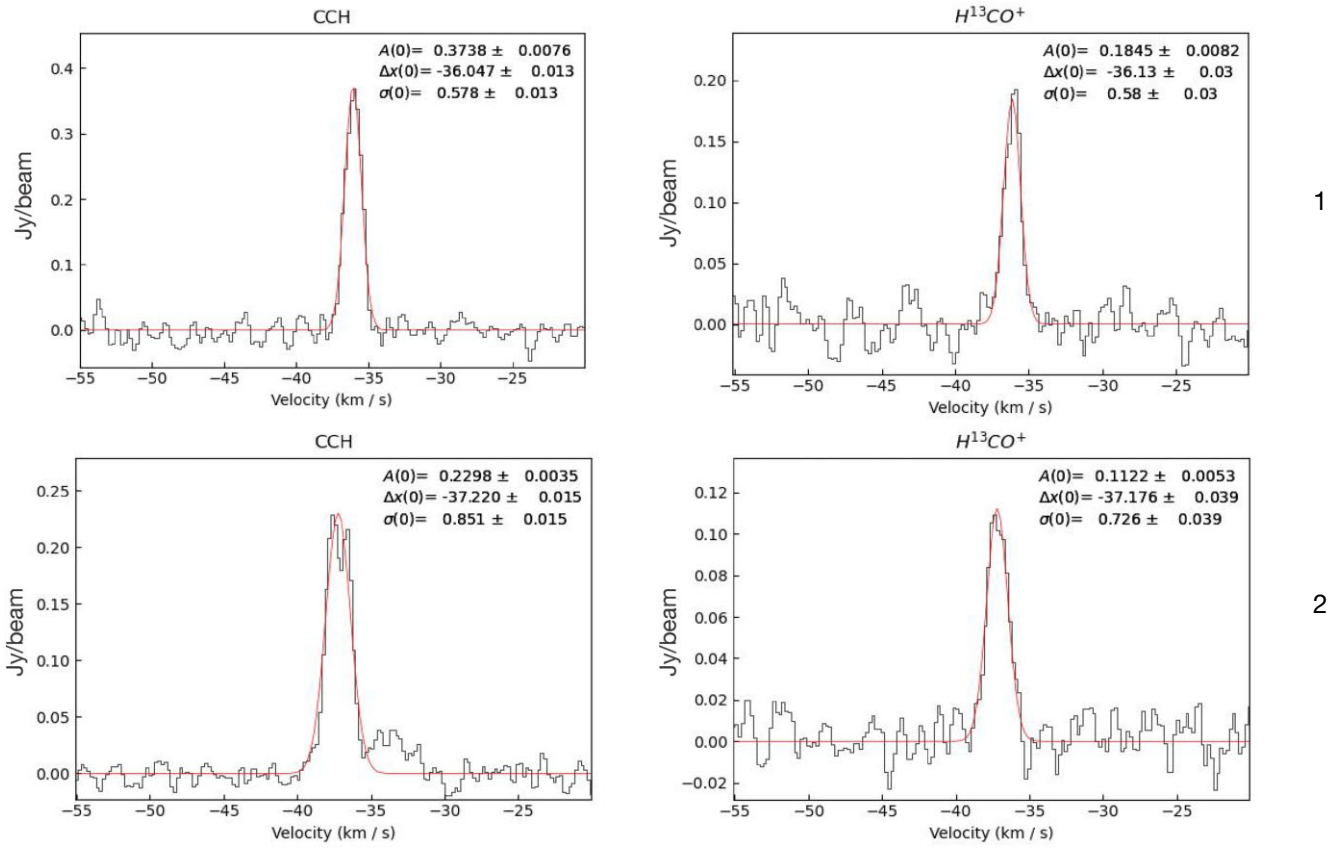

Figure 5. The spectrum of an exemplar source I18461-0113. Left and right panels show the CCH and $H^{13}CO^+$, respectively. The data are shown in black, the Gaussian fits in red.The value and error of Gaussian fits parameters show in the upper right in each panel.

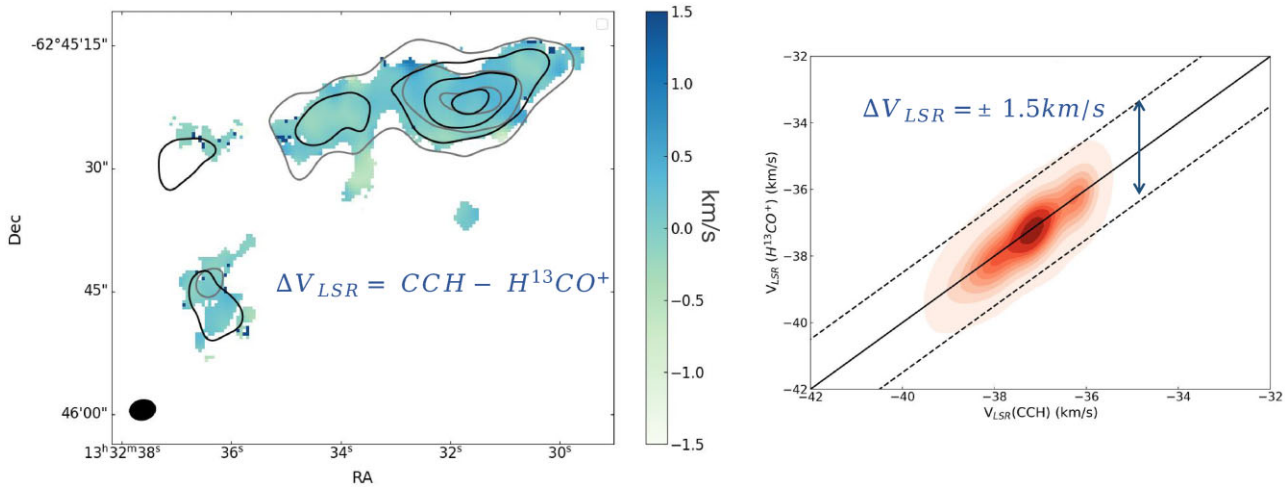

Figure 6. *Left*: Spatial map showing the difference between the ion and neutral centroid velocity (V_{LSR} (CCH) – V_{LSR} ($H^{13}CO^+$)). It shows that CCH presents a smaller centroid velocity than $H^{13}CO^+$. *Right*: Comparison between centroid velocity of CCH and $H^{13}CO^+$, estimated using a two-dimensional KDE. The one-to-one line is marked by the black solid line, as well as offsets of ± 1.5 km s^{-1} with the dotted lines.

confidence interval. The parameter in the histogram at the top left corner represents the spectral peak, while the parameter at the bottom right corner denotes the line width. Fig. 7 shows that under different noise level conditions, the line width error is less than 0.015 km s^{-1}. Therefore, under different noise level conditions, the line width error will not affect the analysis of AD.

When considering the 12-m and ACA visibility data jointly, there is a 20 per cent flux error. Consequently, we also employ corner maps for error analysis in this context. In our data set, the range of peak flux is approximately from 0.15 to 0.3 Jy beam^{-1} km s^{-1}. Therefore, the amplitudes used for Gaussian fitting are 0.1, 0.15, 0.2, 0.25, 0.3, and 0.35 Jy beam^{-1} km s^{-1}. Considering that the impact of peak flux on

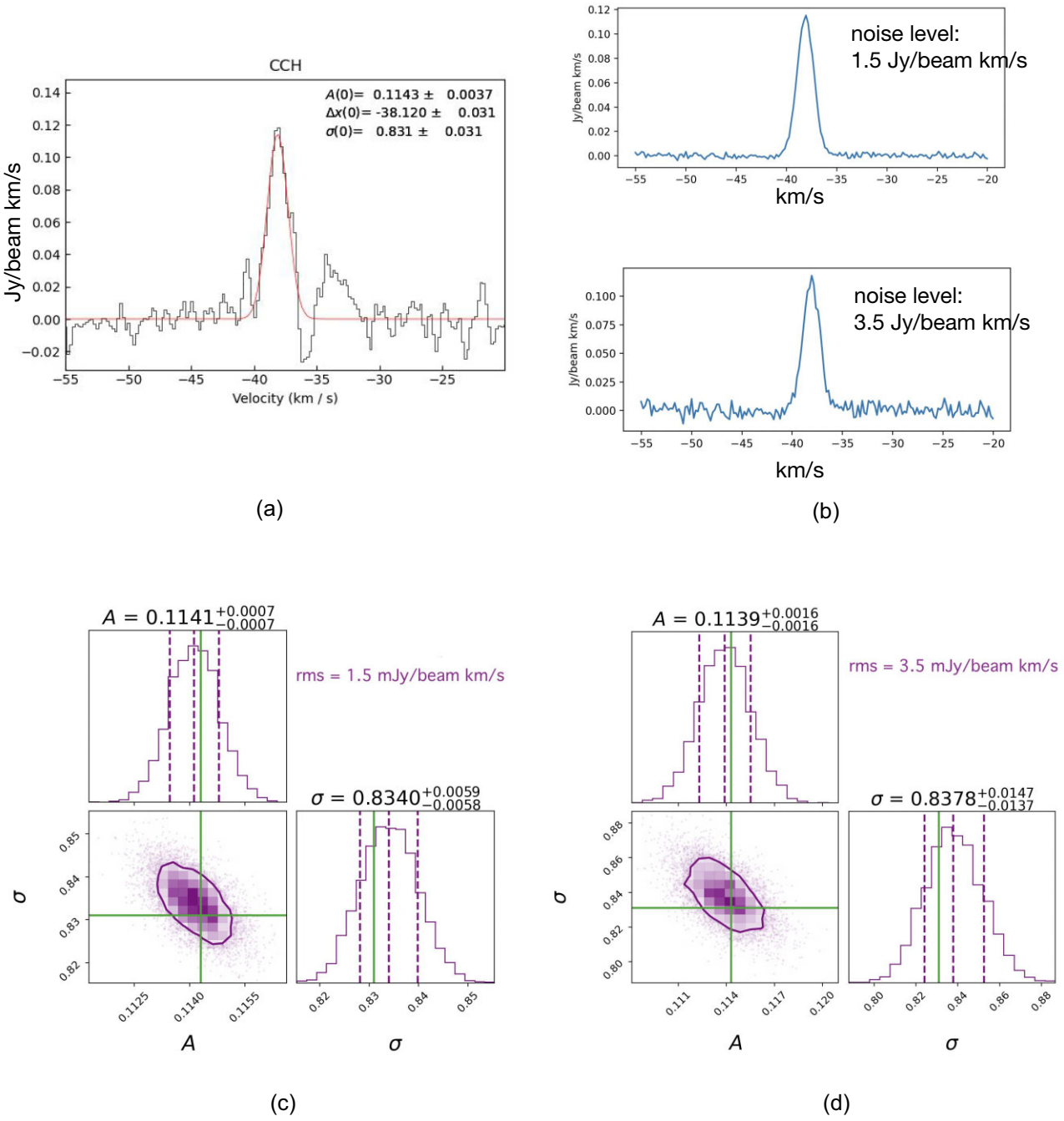

Figure 7. Panel (a) presents the spectrum of CCH. Panel (b) presents the the Gaussian line with added white noise. Panels (c) and (d) present the corner maps. In the corner map, the histogram represents the measure of fit deviation when the parameters are randomly sampled near the best fit. The green solid line indicates the best fit, while the purple dashed lines represent the 16 per cent, 50 per cent (median), and 84 per cent confidence interval percentiles. The subtitles on the histograms display the estimated values for each parameter along with the Gaussian errors at the 68 per cent confidence interval. The parameter in the histogram at the top-left corner represents the spectral peak, while the parameter at the bottom-right corner denotes the line width.

fitting error varies with different line widths, we selected line widths of 0.5, 0.8, and 1.98 km s^{-1} as samples based on the range of line widths, generating 18 Gaussian spectral lines with added white noise at 0.35 mJy beam^{-1} km s^{-1}. Fig. 8 illustrates how the error varies with peak flux for different line widths. The wider the line width, the more significant the influence of peak flux on the error. However, in this data set, the line width error caused by peak flux does not exceed 0.01 km s^{-1}.

Combining these two types of errors using the error propagation formula $\delta^2 = \sqrt{\delta_1^2 + \delta_2^2}$, the total error is calculated to be 0.018 km s^{-1}. Compared to the spectral resolution (approximately 0.2 km s^{-1}) and typical line widths (approximately 1.5 km s^{-1}) for CCH and $H^{13}CO^+$, the uncertainties in the line width measurements are minimal. Generally, the noise level and the 20 per cent flux error will not affect our further comparative analysis of the line widths of CCH and $H^{13}CO^+$.

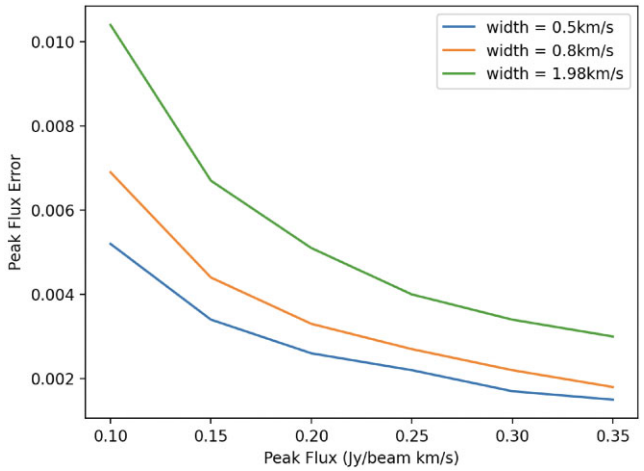

Figure 8. The error varies with peak flux for different line widths. The blue, orange, and green lines represents the line width of 0.5, 0.8, and 1.98 km s^{-1}, respectively.

The velocity dispersion maps for both tracers (CCH and $H^{13}CO^+$) in the exemplar source I13291-6229 are shown in Fig. 9. The velocity dispersion maps for the remaining 11 sources are presented in the online materials. In source I13291-6229, the velocity dispersion maps of both lines show a similar trend that the velocity dispersion is larger in the centre of the core than at the outskirt.

We calculated the mean and standard of the velocity dispersions of $H^{13}CO^+$ and CCH for 12 sources. The parameters are listed in columns four and five in the Table 2, which also include PCA cofficients. We plot the mean $\sigma_v(H^{13}CO^+)$ against the mean σ_v(CCH) of the 12 sources in Fig. 10. The dotted line marks the one-to-one line. It can be seen that the velocity dispersions of the $H^{13}CO^+$–CCH pair agree with each other very well in general.

Table 2. The parameters of 12 sources which selected for analysis of velocity dispersion. The PCA correlation coefficients of CCH–$H^{13}CO^+$ and $H^{13}CN$–$H^{13}CO^+$ pair list in column two and three, respectively. The mean and standard deviation of the velocity dispersions of $H^{13}CO^+$ and CCH are listed in columns four and five.

ID	PCA CCH	PCA $H^{13}CN$	$\sigma_v(CCH)$ (mean ± std) (km s^{-1})	$\sigma_v(H^{13}CO^+)$ (mean ± std) (km s^{-1})
I13291-6229	0.76	0.77	0.92 ± 0.27	0.81 ± 0.25
I13295-6152	0.81	0.68	0.89 ± 0.14	0.98 ± 0.2
I13484-6100	0.91	0.88	1.36 ± 0.45	1.34 ± 0.43
I16272-4837	0.86	0.82	1.08 ± 0.25	1.02 ± 0.26
I16330-4725	0.91	0.90	1.25 ± 0.3	1.26 ± 0.33
I16484-4603	0.84	0.83	1.05 ± 0.38	1.09 ± 0.36
I17143-3700	0.84	0.89	1.37 ± 0.31	1.33 ± 0.31
I17439-2845	0.70	0.73	0.72 ± 0.21	0.74 ± 0.22
I17589-2312	0.79	0.74	1.04 ± 0.33	0.91 ± 0.29
I18223-1243	0.76	0.59	0.77 ± 0.31	0.7 ± 0.33
I18461-0113	0.82	0.90	1.14 ± 0.19	1.18 ± 0.17
I18469-0132	0.79	0.89	1.21 ± 0.27	1.2 ± 0.27

4 DISCUSSION

The comparison of both the morphology of the integrated intensity maps and PCA correlation coefficients suggest that CCH and $H^{13}CO^+$ may trace similar structures in high-mass star-forming regions. Therefore, CCH and $H^{13}CO^+$ could be a good neutral/ion pair for investigating the AD effect.

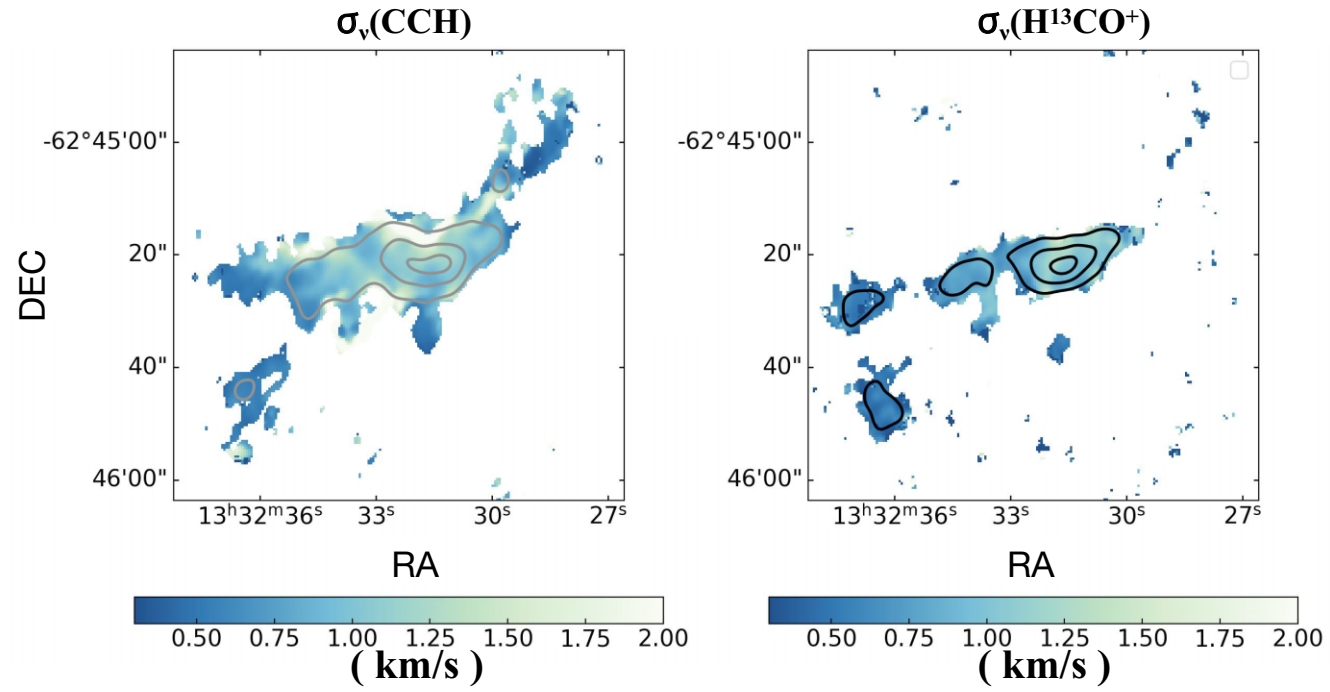

Figure 9. Source I13291-6229. Velocity dispersion maps for CCH and $H^{13}CO^+$ are shown in the left and right panels, respectively. The grey and black contours are shown for the CCH and $H^{13}CO^+$ integrated intensity map, respectively. The contour levels are drawn at 40 per cent, 70 per cent, and 90 per cent of peak values. Each panel's corresponding colour bar delineates the line width values.

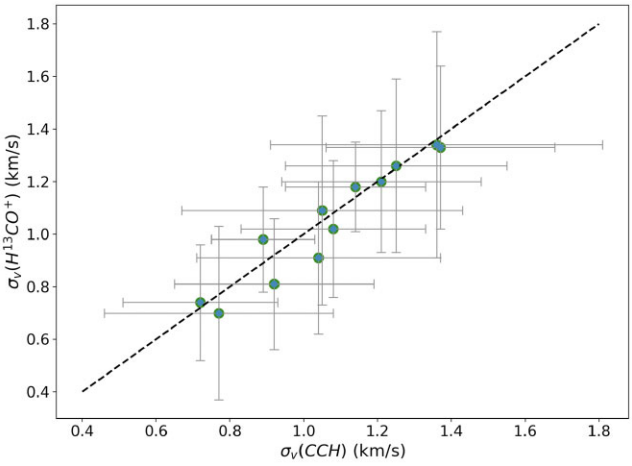

Figure 10. The mean $\sigma_v(H^{13}CO^+)$ against the mean σ_v(CCH) for the selected 12 sources. The dotted line marks an one-to-one line. The error bars show the standard deviation of the velocity dispersions.

In principle, comparison between natural and ion molecules in the line width should be the non-thermal line widths. However, considering the large line widths in high-mass star-forming regions, and the comparable molecule mass of CCH and $H^{13}CO^+$, the effect from thermal component is pretty small. In this paper, we directly use velocity dispersion in the AD analysis because of a lack of gas temperature measurements. We calculated the ratio between the velocity dispersion (σ_v ratio) obtained between CCH and $H^{13}CO^+$ (R(CCH/$H^{13}CO^+$)) for the 12 sources. The left panel of Fig. 11 shows the ratio map of an exemplar source I13291-6229. This map shows that R(CCH/$H^{13}CO^+$) is higher in the outskirt of cores than in the central region, although such a spatial trend is not significant. To better analyse the line widths of tracers, we show the CCH and $H^{13}CO^+$ spectra toward representative regions, which are marked by red circle and numbered in left panel of Fig. 11. The right panel of Fig. 11 shows a direct comparison of the velocity dispersion distributions of the tracers for all pixels in I13291-6229, using KDE. There are three peaks in the KDE map, two of them around 0.6 and 1.1 km s^{-1} show equal velocity dispersion for CCH (neutrals) and $H^{13}CO^+$ (ions). These two peaks correspond to the regions numbered as 4 and 8 in the left panel of Fig. 11. In the third peak of the KDE plot, CCH has a systematically larger (by around 0.25 km s^{-1}) velocity dispersion than $H^{13}CO^+$. This KDE peak is mostly from the regions numbered as 3 and 6 in the left panel of Fig. 11, which are clearly offset from the emission peak.

We show the σ_v ratios (R(CCH/$H^{13}CO^+$)) as a function of the intensity of $H^{13}CO^+$ for the source I13291-6229 in Fig. 12. The figure shows that the velocity dispersion of CCH is in most cases comparable to that of $H^{13}CO^+$, and this remains true also in high-density regions. In contrast, in low-density regions the CCH velocity dispersion tends to be larger than the $H^{13}CO^+$ dispersion. Therefore, if AD is present, it will more likely occur in low-density regions. The left panel in Fig. 11 also shows a similar pattern. Around peak 8, which is in the highest density region, the R(CCH/$H^{13}CO^+$) ratio is lower than the lower density regions such as 6, 7, and 9.

For the remaining sources, we show their intensity maps, velocity dispersion maps, velocity dispersion ratio maps, KDE maps, and σ_v ratio-intensity distribution maps in the online materials. By analysing these maps, one can identify three types of sources.

(i) Sources like I13291-6229, such as I17439-2845, I13484-6100, and I17589-2312. In most cases, the velocity dispersion of CCH is about the same as $H^{13}CO^+$, but in low-density regions, the CCH has a larger velocity dispersion than $H^{13}CO^+$. In high-density regions, there is not much difference in velocity dispersion between the two tracers.

(ii) Sources like I17589-2312. The velocity dispersion of CCH is larger than that of $H^{13}CO^+$ in a large range of densities, as shown in the right panel of Fig. 13. This is similar to the findings in Li et al. (2010). The KDE map in Fig. 14 shows that the ions display a narrower line width in the whole region. In low-density regions, the R(CCH/$H^{13}CO^+$) ratios are even much higher.

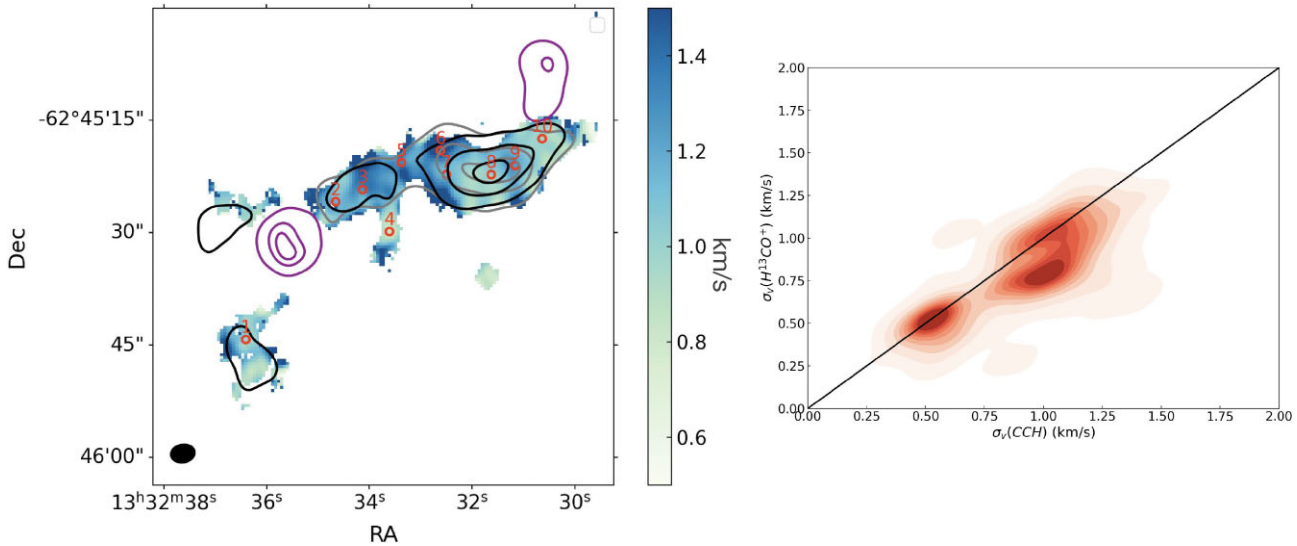

Figure 11. Source I13291-6229. *Left*: Ratio of the velocity dispersion between CCH and $H^{13}CO^+$(R(CCH/$H^{13}CO^+$)). The black, grey, and purple contours are shown for the $H^{13}CO^+$ and CCH integrated intensity map and 3 mm continuum emission, respectively, with levels the same as in Fig. 9. The red circles and numbers show the positions of the sample spectra. In Fig. 5, the spectra for points 1 and 2 are displayed, while the spectra for the remaining points 3 through 10 are available in the online materials. The colour bar delineates the R(CCH/$H^{13}CO^+$) values. *Right*: Comparison between the velocity dispersion of $H^{13}CO^+$ and CCH, estimated using a two-dimensional KDE. The one-to-one line is marked by the black solid line.

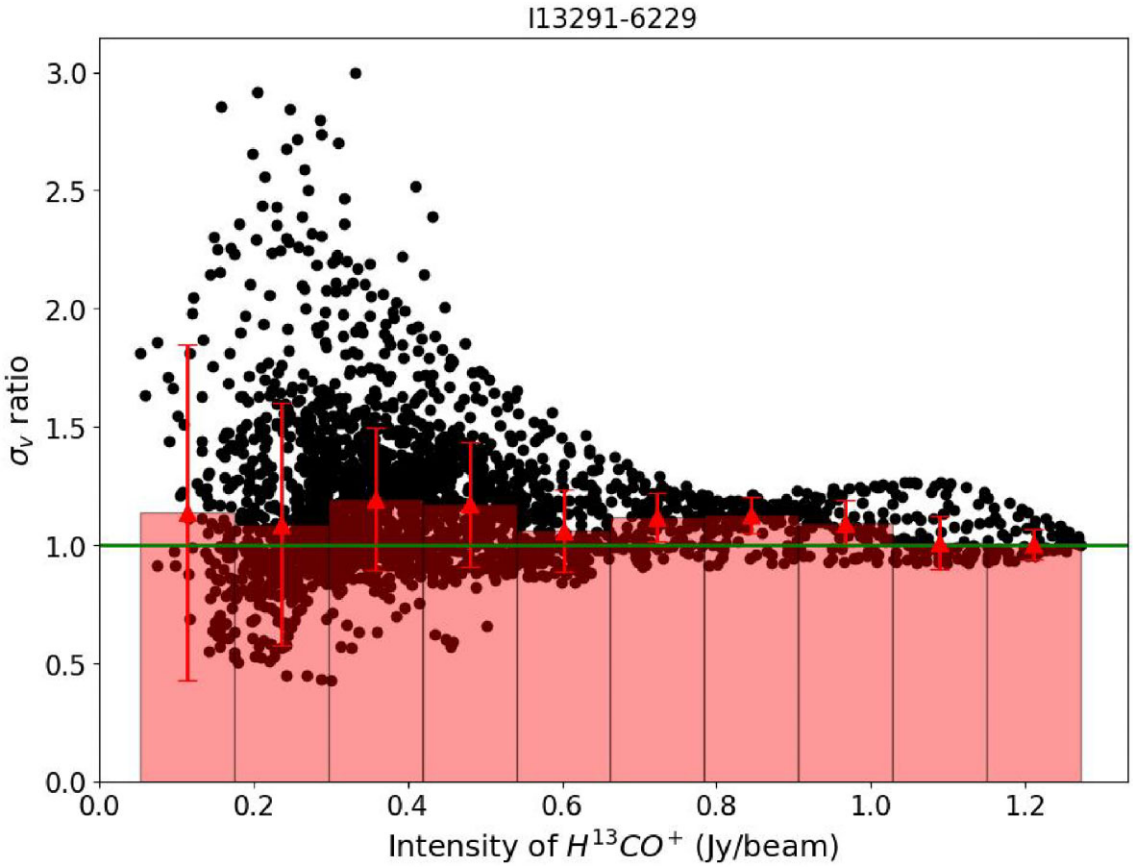

Figure 12. Source I13291-6229. The distribution of the σ_v ratio R(CCH/$H^{13}CO^+$) and the intensity of $H^{13}CO^+$. The width of the red rectangle represents the bins of intensity. The red triangles and error bars represent the median value of σ_v ratio and standard deviation in each bin, respectively. The green line shows that σ_v ratio equal to one.

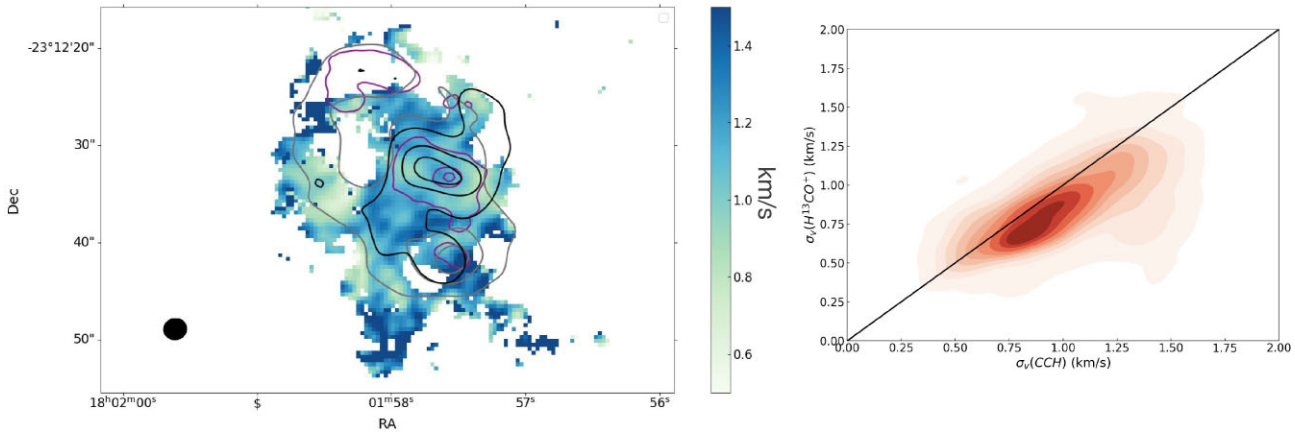

Figure 13. Source I17589-2312. *Left*: Ratio of the velocity dispersion between CCH and $H^{13}CO^+$(R(CCH/$H^{13}CO^+$)). The black and grey contours are shown for the $H^{13}CO^+$ and CCH integrated intensity map, respectively. The contour levels are drawn at 40 per cent, 70 per cent, and 90 per cent of peak values. The purple contour is shown for the 3 mm continuum emission. The contour levels are drawn at 10 per cent, 60 per cent, and 90 per cent of peak values. The colour bar delineates the R(CCH/$H^{13}CO^+$) values. *Right*: Comparison between the velocity dispersion of $H^{13}CO^+$ and CCH, estimated using KDE. The one-to-one line is marked by the black solid line.

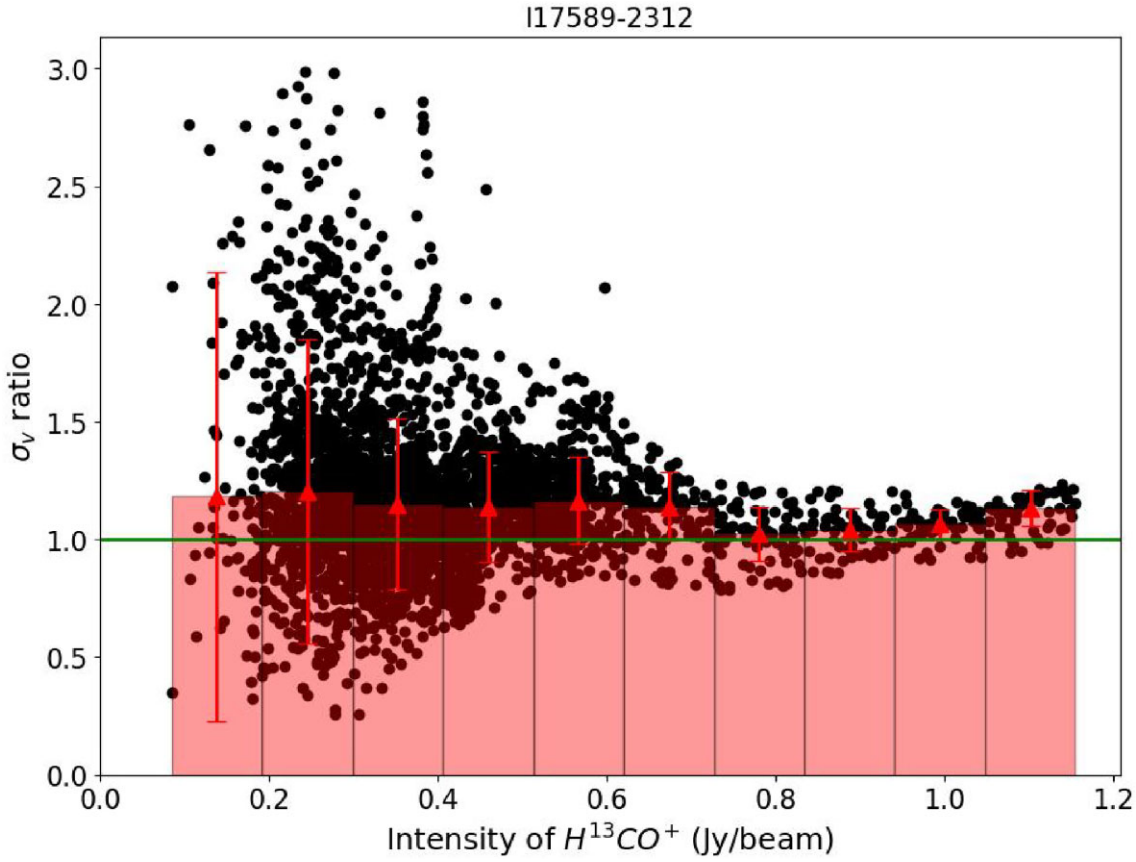

Figure 14. Source I17589-2312, the distribution of the σ_v ratio (R(CCH/$H^{13}CO^+$)) and the intensity of $H^{13}CO^+$. The width of the red rectangle represents the bins of intensity. The red triangles and error bars represent the median value of σ_v ratio and standard deviation in each bin, respectively. The green line shows that σ_v ratio equal to one.

The velocity dispersion of CCH is also larger than that of $H^{13}CO^+$ in source I16272-4837, as shown in the right panel of Fig. 15. However, the R(CCH/$H^{13}CO^+$) ratios are higher in its high-density regions than in its low-density region in Fig. 16, opposite to the source I17589-2312.

(iii) Sources like I16330-4725 as shown in the right panel of Fig. 17. There are two peaks in the KDE map. One shows the CCH having an equal velocity dispersion to $H^{13}CO^+$. While the other peak shows that CCH has lower velocity dispersion than $H^{13}CO^+$. Fig. 18 also shows that in high-density areas CCH has an even smaller velocity dispersion than $H^{13}CO^+$. This situation is similar to the case in the dense core Barnard 5 (Pineda et al. 2021).

It should be noted that Pety et al. (2017) indicates the critical densities for CCH and $H^{13}CO^+$ are similar, which are 1×10^5 and 2×10^5 cm^{-3}, respectively, at a temperature of 30 K. However, Shirley (2015) reports a much lower effective critical density for the $H^{13}CO^+$ line at 20 K, which is approximately 2×10^4 cm^{-3}. Unfortunately, Shirley (2015) did not derive the effective critical density for CCH. However, considering the good correlation of CCH and $H^{13}CO^+$ in their spatial distributions and centroid velocities, CCH and $H^{13}CO^+$ should trace similar density gas at least in the 12 sources that are analysed here.

Overall, the first two types of sources show that the velocity dispersion of CCH is broader than $H^{13}CO^+$ in general. The difference of these two cases is that neutral lines have larger velocity dispersion only in the low-density region in the first type sources, while neutral lines show higher velocity dispersion in the whole emission regions of type 2 sources. The third type sources are opposite to the first two type sources. Their neutral lines have narrower line widths than their ion lines. However, even in type 3 sources, CCH shows a larger velocity dispersion than $H^{13}CO^+$ in a large fraction of pixels in their low-density region.

Fig. 19 shows the σ_v ratios (R(CCH/$H^{13}CO^+$)) as a function of the intensity of $H^{13}CO^+$ for all selected 12 sources. The intensity of $H^{13}CO^+$ is normalized. The maximum and minimum value for normalization is the maximum and minimum intensity of each source. The distribution of velocity dispersions is close to being symmetric for all selected 12 sources. This figure also shows in low-density regions, the CCH has a slightly larger velocity dispersion than $H^{13}CO^+$. While in high-density regions, it shows $H^{13}CO^+$ has a slightly larger velocity dispersion than CCH. We also noticed that dispersion of the σ_v ratios (R(CCH/$H^{13}CO^+$)) is much larger in low-density regions than in high-density regions.

In a word, if high R(CCH/$H^{13}CO^+$) represents active AD, the AD effect may be more significant in some low-density regions of high-mass star-forming regions, which should be further studied with higher quality of data in future. However, considering the large scatter of data points, the AD effect is not significant from a statistical point of view.

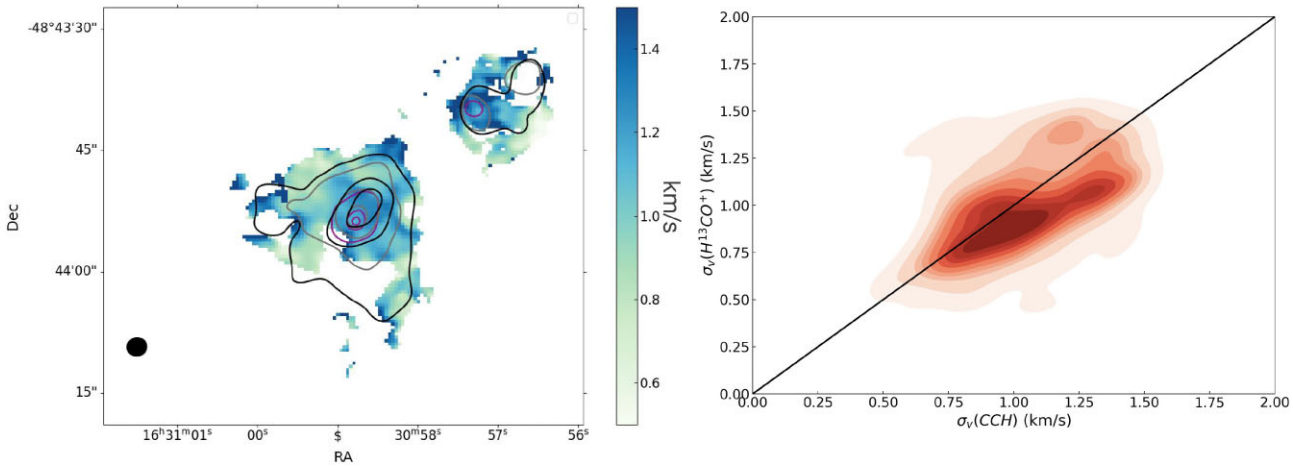

Figure 15. Source I16272-4837. *Left*: Ratio of the velocity dispersion between CCH and $H^{13}CO^+$(R(CCH/$H^{13}CO^+$)). The black and grey contours are shown for the $H^{13}CO^+$ and CCH integrated intensity map, respectively. The contour levels are drawn at 40 per cent, 70 per cent, and 90 per cent of peak values. The purple contour is shown for the 3 mm continuum emission. The contour levels are drawn at 20 per cent, 60 per cent, and 90 per cent of peak values. The colour bar delineates the R(CCH/$H^{13}CO^+$) values. *Right*: Comparison between the velocity dispersion of $H^{13}CO^+$ and CCH, estimated using KDE. The one-to-one line is marked by the black solid line.

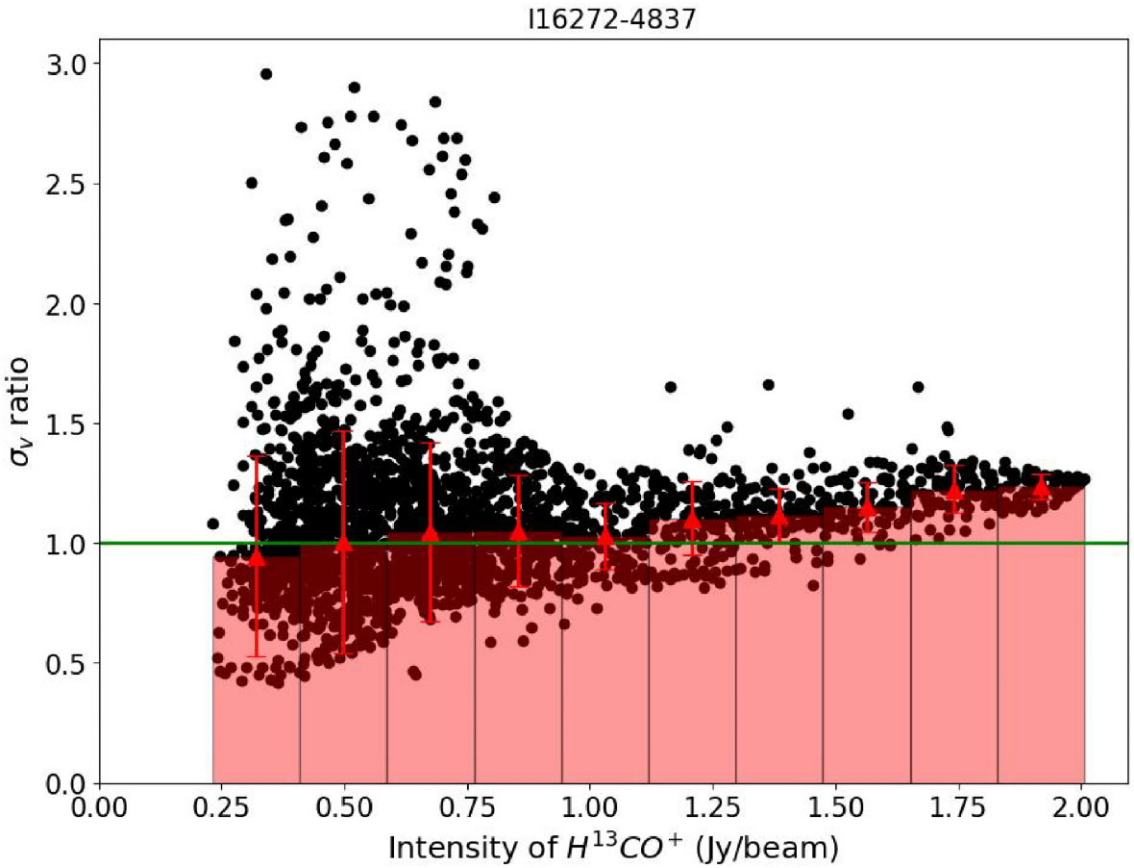

Figure 16. Source I16272-4837, the distribution of the σ_v ratio (R(CCH/$H^{13}CO^+$)) and the intensity of $H^{13}CO^+$. The width of the red rectangle represents the bins of intensity. The red triangles and error bars represent the median value of σ_v ratio and standard deviation in each bin, respectively. The green line shows that σ_v ratio equal to one.

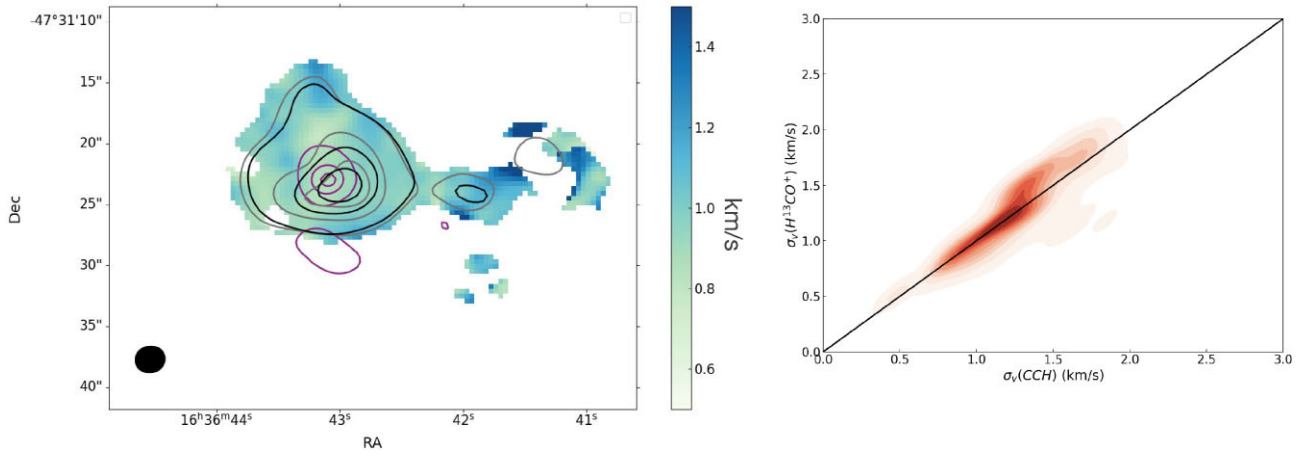

Figure 17. Source I16330-4725. *Left*: Ratio of the velocity dispersion between CCH and $H^{13}CO^+$(R(CCH/$H^{13}CO^+$)). The black and grey contours are shown for the $H^{13}CO^+$ and CCH integrated intensity map, respectively. The contour levels are drawn at 40 per cent, 70 per cent, and 90 per cent of peak values. The purple contour is shown for the 3 mm continuum emission. The contour levels are drawn at 20 per cent, 60 per cent, and 90 per cent of peak values. The colour bar delineates the R(CCH/$H^{13}CO^+$) values. *Right*: Comparison between the velocity dispersion of $H^{13}CO^+$ and CCH, estimated using KDE. The one-to-one line is marked by the black solid line.

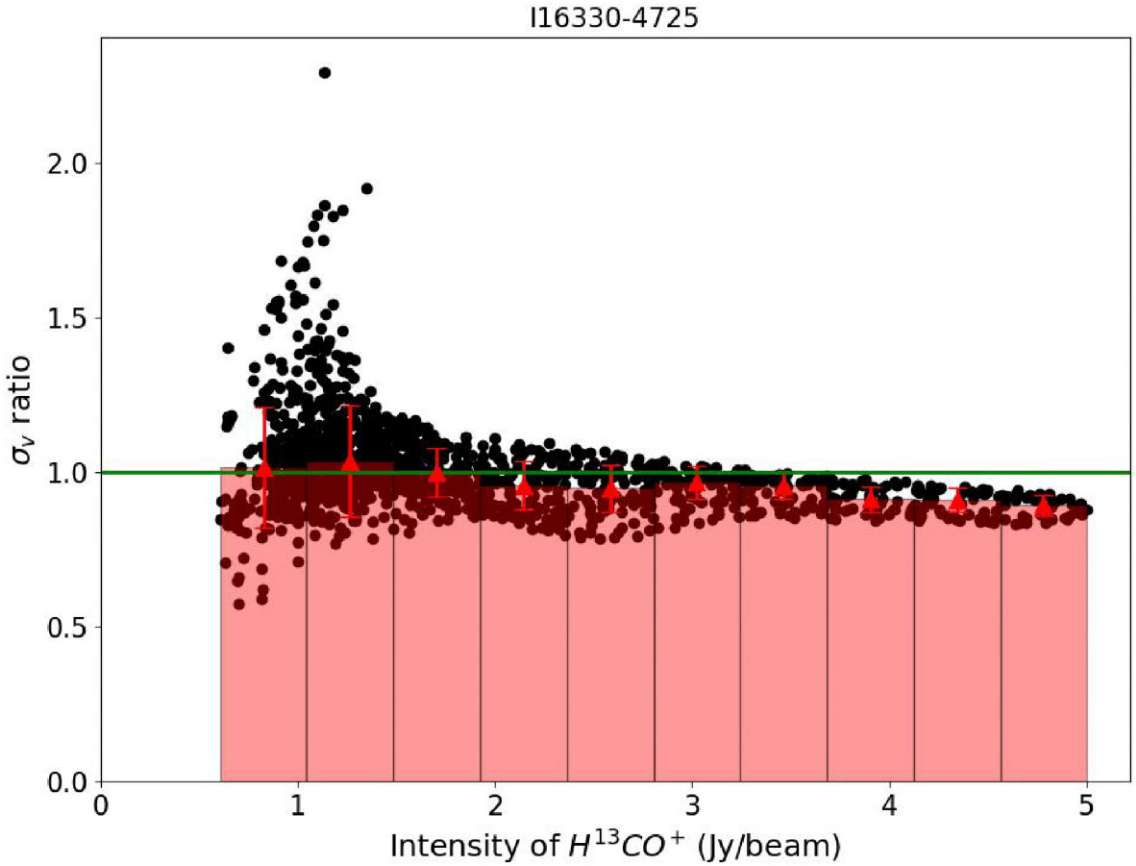

Figure 18. Source I16330-4725, the distribution of the σ_v ratio (R(CCH/$H^{13}CO^+$)), and the intensity of $H^{13}CO^+$. The width of the red rectangle represents the bins of intensity. The red triangles and error bars represent the median value of σ_v ratio and standard deviation in each bin, respectively. The green line shows that σ_v ratio equal to one.

5 CONCLUSION

We presented ATOMS $H^{13}CO^+$, $H^{13}CN$, and CCH line observations of a large sample of massive clumps, and investigated the differences in their velocity dispersions. Our results can be summarized as follows.

(i) We performed PCA analysis on the integrated emission maps of $H^{13}CN$ versus $H^{13}CO^+$ and CCH versus $H^{13}CO^+$ to characterize

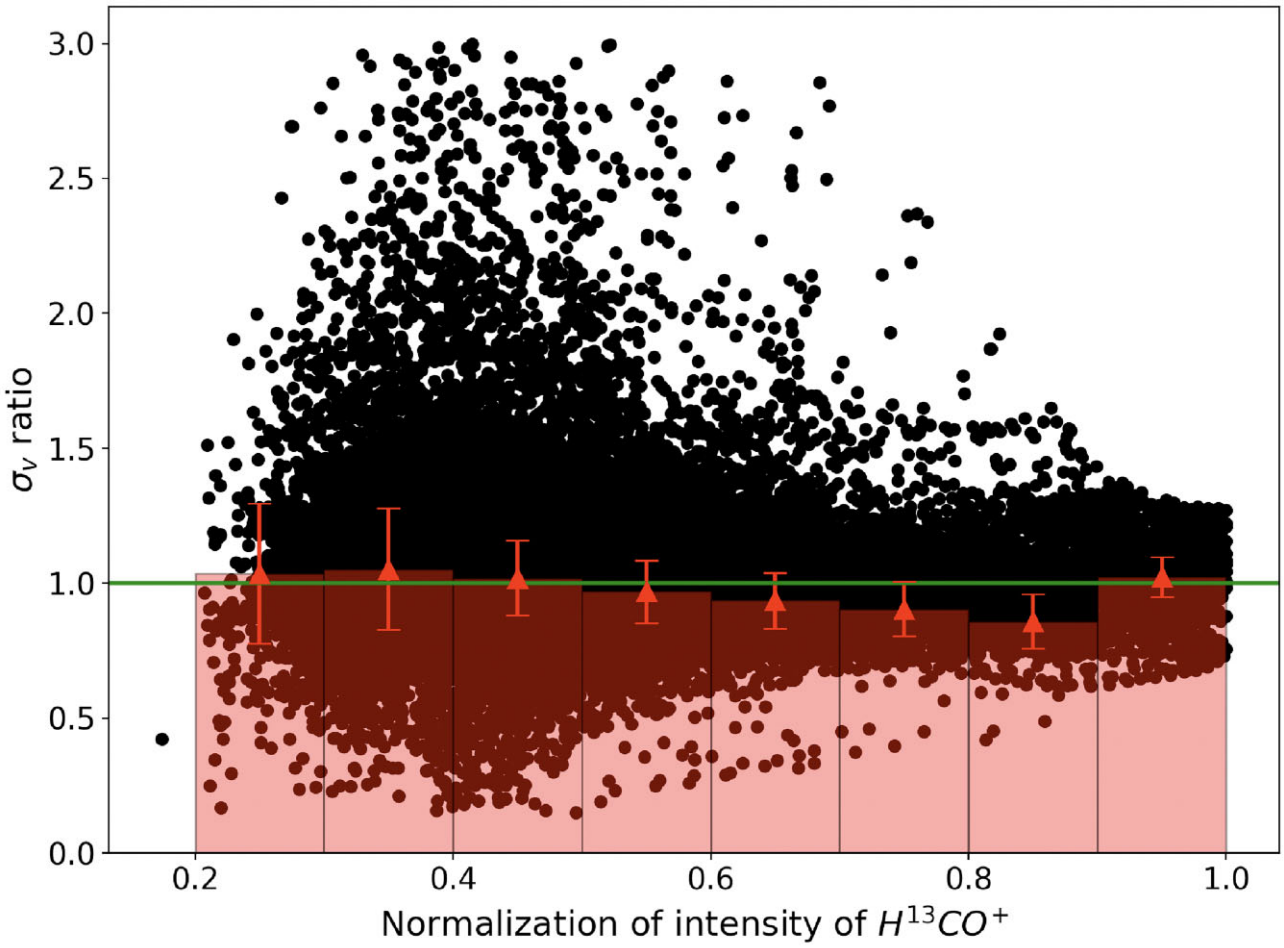

Figure 19. The velocity dispersion ratios, denoted as R(CCH/$H^{13}CO^+$), are presented as a function of the $H^{13}CO^+$ intensity across the 12 selected sources, with the $H^{13}CO^+$ intensity serving as the normalizing factor. The red triangles and error bars represent the median value of σ_v ratio and standard deviation in each bin, respectively. The green line shows that σ_v ratio equal to one.

their differences in spatial distributions. These three molecular lines show very similar large-scale spatial distributions and are strongly correlated with each other in spatial distributions. We found that $H^{13}CN$ shows a slightly stronger correlation with $H^{13}CO^+$ compared to CCH.

(ii) We picked out 12 sources out of the 62 sources, where CCH and $H^{13}CO^+$ don't show correlation with the outflows and dominated by one velocity component, for studying the AD effect by measuring the velocity dispersion of CCH and $H^{13}CO^+$ as a neutral/ion pair. We find that CCH shows larger velocity dispersion than $H^{13}CO^+$ in low-density regions of most sources, which indicates that AD effect is more significant in low-density gas if AD is present.

ACKNOWLEDGEMENTS

This work has been supported by the National Key R&D Program of China (No. 2022YFA1603100). TL acknowledges support from the National Natural Science Foundation of China (NSFC), through grant Nos 12073061 and 12122307, the Tianchi Talent Program of Xinjiang Uygur Autonomous Region, and the international partnership programme of the Chinese Academy of Sciences, through grant No. 114231KYSB20200009. Z-YR acknowledges support from the NSFC grant (No. 11988101). H-LL was supported by Yunnan Fundamental Research Project (grant Nos 202301AT070118, and 202401AS070121), and by Xingdian Talent Support Plan–Youth Project. CWL was supported by the Basic Science Research Program through the NRF funded by the Ministry of Education, Science and Technology (NRF- 2019R1A2C1010851) and by the Korea Astronomy and Space Science Institute grant funded by the Korea government (MSIT; project No. 2024-1-841-00). SRD acknowledges support from the Fondecyt Post-doctoral fellowship (project code 3220162) and ANID BASAL project FB210003. LB gratefully acknowledges support by the ANID BASAL project FB210003. MJ acknowledges the support of the Research Council of Finland Grant No. 348342. KT was supported by JSPS KAKENHI (Grant Number JP20H05645). This paper makes use of the following ALMA data: ADS/JAO.ALMA#2019.1.00685.S. ALMA is a partnership of ESO (representing its member states), NSF (USA), and NINS (Japan), together with NRC (Canada), MOST and ASIAA (Taiwan), and KASI (Republic of Korea), in cooperation with the Republic of Chile. The Joint ALMA Observatory is operated by ESO, AUI/NRAO, and NAOJ. DL is a New Cornerstone Investigator.

DATA AVAILABILITY

The raw data are available in ALMA archive. The derived data underlying this article are available in the article and in its online supplementary material.

REFERENCES

Bronfman L., Nyman L. A., May J., 1996, A&AS, 115, 81
Fatuzzo M., Adams F. C., 2002, ApJ, 570, 210
Heitsch F., Zweibel E. G., Slyz A. D., Devriendt J. E. G., 2004, ApJ, 603, 165
Hezareh T., Houde M., McCoey C., Li H.-b., 2010, ApJ, 720, 603
Hezareh T., Csengeri T., Houde M., Herpin F., Bontemps S., 2014, MNRAS, 438, 663
Houde M., Bastien P., Peng R., Phillips T. G., Yoshida H., 2000, ApJ, 536, 857
Jones P. A. et al., 2012, MNRAS, 419, 2961
Jones P. A., Burton M. G., Cunningham M. R., Tothill N. F. H., Walsh A. J., 2013, MNRAS, 433, 221
Klaassen P. D., 2008, PhD thesis, McMaster Univ., Canada
Li H.-b., Houde M., 2008, ApJ, 677, 1151
Li H.-b., Houde M., Lai S.-p., Sridharan T. K., 2010, ApJ, 718, 905
Liu T. et al., 2016, ApJ, 829, 59
Liu T. et al., 2020a, MNRAS, 496, 2790
Liu T. et al., 2020b, MNRAS, 496, 2821
Liu H.-L. et al., 2021, MNRAS, 505, 2801
Lo N. et al., 2009, MNRAS, 395, 1021
Mouschovias T. C., 1987, in Morfill G. E., Scholer M., eds, NATO Advanced Study Institute (ASI) Series C Vol. 210, Physical Processes in Interstellar Clouds. D. Reidel Publishing Co., Dordrecht, p. 453
Mouschovias T. C., Tassis K., 2008, preprint (arXiv:0807.4571)
Nakamura F., Li Z.-Y., 2005, ApJ, 631, 411
Pety J. et al., 2017, A&A, 599, A98
Pineda J. E., Schmiedeke A., Caselli P., Stahler S. W., Frayer D. T., Church S. E., Harris A. I., 2021, ApJ, 912, 7
Shirley Y. L., 2015, PASP, 127, 299
Sokolov V. et al., 2019, ApJ, 872, 30
Tafalla M., Myers P. C., Caselli P., Walmsley C. M., 2004, A&A, 416, 191
Tang K. S., Li H.-B., Lee W.-K., 2018, ApJ, 862, 42
Xu F.-W. et al., 2023, MNRAS, 520, 3259
Zhou J.-W. et al., 2022, MNRAS, 514, 6038
Zweibel E. G., 2002, ApJ, 567, 962

SUPPORTING INFORMATION

Supplementary data are available at MNRAS online.

suppl_data

Please note: Oxford University Press is not responsible for the content or functionality of any supporting materials supplied by the authors. Any queries (other than missing material) should be directed to the corresponding author for the article.

[1]*Department of Physics, Taiyuan Normal University, Jinzhong 030619, China*
[2]*Institute of Computational and Applied Physics, Taiyuan Normal University, Jinzhong 030619,China*
[3]*Shanghai Astronomical Observatory, Chinese Academy of Sciences, 80 Nandan Road, Shanghai 200030, China*
[4]*National Astronomical Observatories, Chinese Academy of Sciences, Beijing 100012, China*
[5]*Research Center for Intelligent Computing Platforms, Zhejiang Laboratory, Hangzhou 311100, China*
[6]*School of Physics and Astronomy, Yunnan University, Kunming 650091, China*
[7]*Kavli Institute for Astronomy and Astrophysics, Peking University, 5 Yiheyuan Road, Haidian District, Beijing 100871, China*
[8]*University of Chinese Academy of Sciences, School of Astronomy and Space Science, Beijing 100049, People's Republic of China*
[9] *Department of Astronomy, Tsinghua University, Beijing 100084, China*
[10]*Research Center For Astronomical Computing, Zhejiang Laboratory, Hangzhou 311100, China*
[11]*Nobeyama Radio Observatory, National Astronomical Observatory of Japan, Nobeyama, Minamimaki, Minamisaku, Nagano 384-1305, Japan*
[12]*Astronomical Science Program, Graduate Institute for Advanced Studies, SOKENDAI, 2-21-1 Osawa, Mitaka, Tokyo 181-8588, Japan*
[13]*Department of Physics, University of Helsinki, PO Box 64, FI-00014 Helsinki, Finland*
[14]*Korea Astronomy and Space Science Institute, 776 Daedeokdaero, Yuseong-gu, Daejeon 4055, Republic of Korea*
[15]*University of Science and Technology, Korea (UST), 217 Gajeong-ro, Yuseong-gu, Daejeon 34113, Republic of Korea*
[16]*Departamento de Astronomí a, Universidad de Chile, Casilla 36-D, 8320168 Santiago, Chile*
[17]*Max-Planck-Institut für Radioastronomie, Auf dem Hügel 69, D-53121 Bonn, Germany*
[18]*Physikalisches Institut, Universität zu Köln, Zülpicher Str. 77, D-50937 Köln, Germany*
[19]*Kavli Institute for Astronomy and Astrophysics, Peking University, Beijing 100871, China*
[20]*Department of Astronomy, School of Physics, Peking University, Beijing 100871, China*
[21]*Indian Institute of Space Science and Technology, Thiruvananthapuram 695547, Kerala, India*
[22]*Indian Institute of Astrophysics, Koramangala, Bangalore 560034, India*
[23]*Department of Mathematical Sciences, University of South Africa, Cnr Christian de Wet Rd and Pioneer Avenue, Florida Park, 1709 Roodepoort, South Africa*
[24]*Centre for Space Research, North-West University, Potchefstroom Campus, Private Bag X6001, Potchefstroom 2520, South Africa,*
[25]*Department of Physics and Astronomy, Faculty of Physical Sciences, University of Nigeria, Carver Building, 1 University Road, Nsukka 410001, Nigeria*

This paper has been typeset from a TEX/LATEX file prepared by the author.